

Characterization of a Quadrotor Unmanned Aircraft System for Aerosol-Particle-Concentration Measurements

James M. Brady,[†] M. Dale Stokes,[‡] Jim Bonnardel,[§] and Timothy H. Bertram^{*,†}

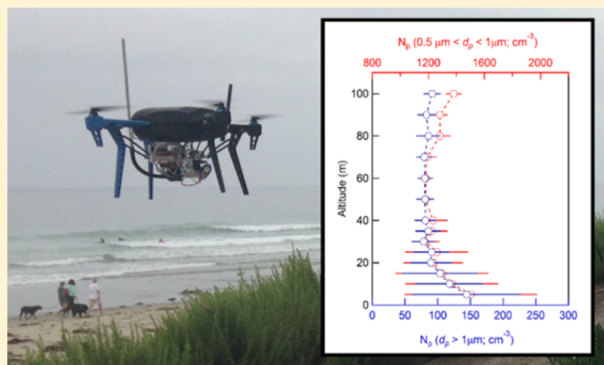
[†]Department of Chemistry, University of Wisconsin, Madison, 53706 Wisconsin, United States

[‡]Scripps Institution of Oceanography, La Jolla, 92037 California, United States

[§]Radio Control Specialties, San Diego, California 92111, United States

Supporting Information

ABSTRACT: High-spatial-resolution, near-surface vertical profiling of atmospheric chemical composition is currently limited by the availability of experimental platforms that can sample in constrained environments. As a result, measurements of near-surface gradients in trace gas and aerosol particle concentrations have been limited to studies conducted from fixed location towers or tethered balloons. Here, we explore the utility of a quadrotor unmanned aircraft system (UAS) as a sampling platform to measure vertical and horizontal concentration gradients of trace gases and aerosol particles at high spatial resolution (1 m) within the mixed layer (0–100 m). A 3D Robotics Iris+ autonomous quadrotor UAS was outfitted with a sensor package consisting of a two-channel aerosol optical particle counter and a CO₂ sensor. The UAS demonstrated high precision in both vertical (± 0.5 m) and horizontal positions (± 1 m), highlighting the potential utility of quadrotor UAS drones for aerosol- and trace-gas measurements within complex terrain, such as the urban environment, forest canopies, and above difficult-to-access areas such as breaking surf. Vertical profiles of aerosol particle number concentrations, acquired from flights conducted along the California coastline, were used to constrain sea-spray aerosol-emission rates from coastal wave breaking.



1. INTRODUCTION

Atmospheric aerosol particles play a central role in Earth's radiation budget,¹ act to limit visibility through the scattering and absorption of radiation,² enable the spreading of biological organisms and pathogens,³ and present a significant health hazard in urban environments.^{4–6} Aerosol particles are generated from both natural and anthropogenic sources and are emitted directly into the atmosphere as primary particles or formed in the atmosphere by gas-to-particle conversion. Ground-based, aircraft, and satellite remote-sensing techniques have been utilized extensively to characterize the emission, chemical and physical transformation, and removal of aerosol particles in Earth's atmosphere. Information on particle spatial distributions comes largely from routine ground-based observations of aerosol particle mass loadings and satellite observations of aerosol optical thickness (AOT). Despite decades of aircraft measurements of aerosol particle number and mass distributions, large uncertainties still exist in our understanding of the vertical distribution of aerosol particles near the surface⁷ and the spatial and temporal variability in particle concentrations on the city scale. As a result, our ability to predict how changes in emissions will impact particle number and mass distributions may be limited by the spatial and temporal resolution of existing measurements within the lower troposphere.^{1,3,7} In this manuscript, we assess the

potential of unmanned aircraft systems (UAS) to meet this measurement need.

The planetary boundary layer (PBL) constitutes the lowestmost region of the troposphere in which flow is strongly influenced by interaction with the surface, responding to surface forcings with a time scale of 1 h or less.⁸ Surface heating results in a turbulent, well-mixed boundary layer during the day in which surface heating can sustain high boundary layer heights (ca. 1–3 km). Deep surface cooling after sunset creates a much shallower stable nocturnal boundary layer (ca. 100–200 m) in which the remainder of the daytime PBL is decoupled from the surface layer, forming a nocturnal residual layer.⁸ Within the PBL, the vertical concentration profiles of aerosols and trace gases are normally nonlinear as a result of natural air turbulence caused by wind shear and temperature gradients.⁹ At present, there are few measurements of aerosol and trace-gas concentration gradients within the lowest 300 m of the PBL. Accurate assessment of the degree to which surface measurements represent the entire PBL are required for validation of remote sensing techniques for surface-air-quality predictions.¹⁰

Received: October 29, 2015

Revised: December 27, 2015

Accepted: January 5, 2016

Current research initiatives, such as NASA's Deriving Information on Surface Conditions from Column and Vertically Resolved Observations Relevant to Air Quality (DISCOVER-AQ) project,¹¹ demonstrate the necessity to constrain aerosol and trace gas profiles within the troposphere for improved interpretation of satellite observations which will improve the accuracy with which near-surface air quality conditions can be diagnosed from space.

Capturing the spatial and temporal variability of aerosol particles and trace gases between the surface and 300 m is currently limited by the sampling platforms with which routine measurements can be made. High spatial resolution measurements of particle number and mass distributions above the surface but below 300m are limited to sampling platforms that can perform controlled horizontal and vertical translations. These measurements are even more restricted within the dense, complex, and constantly evolving nature of urban environments. Current measurement platforms that allow for the vertical profiling of the lower troposphere include fixed tall towers,^{12,13} research vessels over open ocean waters,^{14,15} tethered balloons,¹⁶ winged UASs,^{17–20} large scale research aircraft,^{21–23} and zeppelins.²⁴ Recent advancements in quadrotor UAS technology present an attractive, low-cost alternative for sampling the lower troposphere due to their ability to translate in both the horizontal and vertical dimensions and to hold a fixed position in the atmosphere even under high-wind conditions. Commercial quadrotor UAS can be flown autonomously with preprogrammed electronic flight plans. Here, we characterize a commercial quadrotor UAS as a sampling platform to measure vertical and horizontal profiles of aerosol particle and CO₂ concentrations at a coastal site in Southern California.

Beyond the aforementioned engineering focus, we use the observations obtained here to constrain sea-spray aerosol generation in the surf zone. The generation of marine aerosol particles by processes associated with breaking surface waves and the formation of bubble plumes and foams has been studied extensively in both the laboratory and field.^{25–29} Recent studies have demonstrated that the surf-zone, characterized by abundant wave breaking, is a high-intensive production zone for sea spray aerosol (SSA) relative to the near open ocean.^{30,31} Further work has been dedicated to characterizing a surf source function; Chomka and Petelski³² suggest a function relating the total aerosol flux to wave energy dissipation (WED) to the ³/₄ power, whereas Clarke et al.¹³ calculated a universal function for the surface flux of aerosols for a whitecap coverage of 100% that scales with the whitecap coverage. Although the surf source function is still an area of relatively high uncertainty, assessment of surf aerosol effects is also dependent on the transport of aerosols both horizontally and vertically within the boundary layer, an area in which the literature is even sparser.³³ Hooper and Martin³⁴ used LIDAR to demonstrate surf-aerosol plumes as high as 20 m above sea level, with de Leeuw et al.³¹ later reporting similar plume heights of 20–25 m, inferred from gradient functions based on in situ measurements made at 5 and 15 m above sea level. Clarke et al.¹³ utilized a 20 m tower to collect aerosol samples at 5, 10, and 20 m above sea level and, on the basis of their observations, suggest that the aerosol plumes generated in the surf zone did not exceed 5 m. Assessing the vertical transport of sea spray aerosol within the first 100 m of the boundary layer provides a solid framework for an initial assessment of the novel quadrotor UAS sampling platform as a means for aerosol concentration measurements

within the lower portion of the boundary layer that is currently not assessable by research aircraft, with the exception of missed approaches conducted at airports.

2. MATERIALS AND METHODS

2.1. UAS Sampling Platform. Measurements of particle number concentrations ($d_p > 500$ nm) and CO₂ within the boundary layer at various vertical and horizontal locations were made by mounting two commercial sensors to a 3D Robotics Iris+ autonomous quadcopter (Iris), shown in Figure 1. The

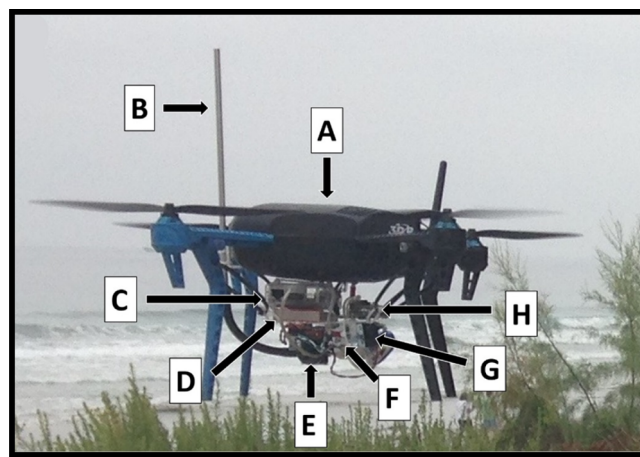


Figure 1. An in-flight photograph of the Iris (A) and sensor package, demonstrating the relative locations of the sampling inlet (B), the Raspberry Pi 1 Model B computer (C), the Mophie powerstation (D), the OEM MetOne particle counter (E), the CO₂Meter K-30 sensor (F), the Energizer Lithium 9 V battery (G), and the Sensidyne micro air pump (H).

Iris measures 20.3 cm in height and 44.5 cm in width and has a span of 50.8 cm with an all-up weight of 1.5 kg. The Iris uses two 10 × 4.7 push propellers and two 10 × 4.7 puller propellers powered by 850 kV motors to create lift and provide maneuverability for the platform. The telemetry range of the Iris is 1 km, more than sufficient to cover the desired sampling window (5–100 m). The Iris is powered by a three-cell, 11.1 V, 3.5 Ah lithium polymer battery providing a flight time of 10–13 min at the manufacturer suggested payload capacity of 400 g. During this study, sampling flights were flown with a forward speed of ca. 24.14 km/h with 15–40 s holds at each waypoint depending on the flight path flown (Table 1). The total top ground speed for the Iris is ca. 56.33 km/h in GPS mode or 72.42 km/h in non GPS mode. The exact flight time achieved is highly dependent on the weight and size of the attached sensor package and is further discussed in section 3.1.

The Iris can be flown either manually or autonomously. As an added safety precaution and to account for the unpredictability of a beach environment, initial take-offs and landings were performed using the manual flight mode. Once airborne, the UAS was switched into fully autonomous mode, wherein the Iris executes a stored mission, progressing through a series of waypoint commands. The waypoints are GPS-positioned points that describe the three-dimensional location of the drone at that point in the flight path, with a latitude, longitude, altitude, and waypoint tolerance. The waypoint commands detail the action of the drone with respect to said waypoint and range along a simple navigation path, including translation and stationary waiting (during sampling). Repre-

Table 1. Flight Plans for the Four Vertical Flight Profiles That Were Utilized during This Study

flight plan A			flight plan B			flight plan C			flight plan D		
waypoint	altitude (m)	hold time (s)	waypoint	altitude (m)	hold time (s)	waypoint	altitude (m)	hold time (s)	waypoint	altitude (m)	hold time (s)
1	5	15	1	3	15	1	4	20	1	5	40
2	10	15	2	6	15	2	8	20	2	10	40
3	20	15	3	9	15	3	12	20	3	20	40
4	30	15	4	12	15	4	16	20	4	30	40
5	40	15	5	15	15	5	20	20	5	40	40
6	50	15	6	18	15	6	24	20			
7	60	15	7	21	15	7	28	20			
8	70	15	8	24	15	8	32	20			
9	80	15	9	27	15	9	36	20			
10	90	15	10	30	15	10	40	20			
11	100	15	11	33	15						
	12	36	15								
	13	39	15								
	14	42	15								

sentative vertical and horizontal flight paths are shown in the [Supporting Information](#), and detailed descriptions of the flight plans flown during this study are provided in [Table 1](#).

The waypoints and flight plans for each flight were programmed using the open-source Mission Planner software. Mission Planner is a full-featured ground station for the ArduPilot Mega (APM) autopilot platform developed by Michael Osborne.³⁵ The Mission Planner software provides an intuitive and simple interface with which autonomous flight paths can be planned, saved, and uploaded into the UAS. In addition to planning the specific flight paths, Mission Planner allows for continuous, real-time monitoring of the status of the Iris during operation. Telemetry logs for all of the flights are recorded and processed by Mission Planner, providing easy access to information such as altitude, acceleration, ground speed, latitude, longitude, roll, and pitch. The on-board autopilot records flight log data at approximately 7 Hz, providing a detailed log of the aircraft's sampling profile post flight.

At the time of this manuscript preparation, the U.S. Federal Aviation Administration (FAA) is undergoing a revision of its policy to govern the use of small unmanned aerial systems (drones) of the type used here for academic research. Currently, the use of small (<25 kg) drones are restricted to visual line-of-sight daylight operation, with a maximum altitude of 150 m and additional restrictions on their operation near controlled airspace (i.e., airports) or above any persons. To the best of our understanding, under present terms, the use of small drones for research is not permitted by the FAA unless the academic institution is granted a permitted exemption certificate for their use. For the purpose of meeting FAA regulations, the UAS used here was operated by an experienced drone pilot (Radio Control Specialties) who possessed a license for commercial UAS operation as well as appropriate liability insurance.

2.2. Sensor Packaging. The optical particle counter (OPC) used in this study is an OEM version of the MetOne 80080 two-channel particle counter. Briefly, the 80080 particle counter uses scattered light from a 670 nm laser to detect and count particles into two predetermined size ranges. The OPC was calibrated using atomized polystyrene microspheres of known size (0.3–1 μm). From the laboratory calibration, the diameter ranges for the OPC were set at $0.5 < d_p < 1 \mu\text{m}$

(channel one) and greater than 1 μm (channel two). The averaging rate was set at 1 Hz. The CO₂ sensor used was a CO₂Meter K-30 sensor. The K30 is a low-cost, low-power CO₂ meter that utilizes nondispersive infrared (NDIR) waveguide technology and an automatic background calibration algorithm to detect CO₂ between 0 and 10 000 ppm. The K-30 has a precision of ± 20 ppm and $\pm 1\%$ of measured value, with an accuracy of ± 30 ppm and $\pm 3\%$ of measured value within specifications. Although originally designed as a diffusion-type sensor, incorporation of the CM-0114 tube-cap adapter kit to the K-30 transforms the sensor into a remote sensor capable of actively measuring CO₂ levels in ambient air samples in real time.

The OEM MetOne particle counter and CO₂ sensor were controlled with a Raspberry Pi 1 Model B computer running a custom Python script. At the start of each sampling flight, the Python script initializes the sensors and begins an 8 min sampling period, during which particle and CO₂ measurements are continuously recorded. The 8 min sampling window was chosen to account for any potential delays in flight start time to ensure that the sample flight window would be captured.

A Sensidyne A120INSNF63VN1 micro air pump provided sample flow for both the MetOne particle counter and K-30 CO₂ sensor. Powered using an Energizer LA522 Advanced lithium 9 V battery, the micro air pump provided a consistent sample flow of 4.88 standard liters per minute (slpm) through both sensors for the duration of each sample flight. Although tests on the battery power demonstrated a constant sample flow for time periods greater than 1 h, the lithium 9 V batteries were replaced every two sample flights to ensure consistent sample flow across all sampling flights.

The components of this sensor package require relatively low power. As previously mentioned, the Metone particle counter and Sensidyne pump were powered with the Energizer lithium 9 V battery and a Mophie powerstation (4000 mAh) was used to provide continuous power to the Raspberry Pi and CO₂ sensor over the entire respective sampling period. All of the individual components were assembled together into a compact package that weighed 490 g. The entire unit was mounted to the undercarriage of the Iris with a sampling inlet mounted to the front of the drone extending approximately 25 cm above the rotors to avoid sampling contamination.

3. RESULTS AND DISCUSSION

3.1. Performance of the Drone Sampling Platform.

Total UAS flight time is critically dependent on the weight of the sensor package. The manufacturer (3D robotics) recommends a payload of 400 g for flight times of 10–13 min, with flight times of 18–20 min possible without a payload attached. The sensor package, inlet tube, and mounting hardware used during this study weighed a total of 510 g, 28% heavier than the recommended payload. At 510 g, we achieved a flight time of 5 min. Figure 2 depicts the nonlinear

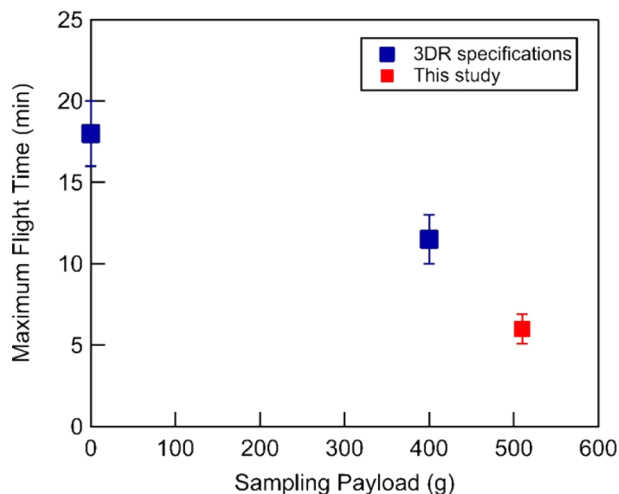


Figure 2. Dependence of UAS flight time on payload weight. Blue squares are flight durations based on 3DR specifications, and the red square is based on the observed flight durations in this study for a 510 g payload.

dependence of the Iris' flight time on payload weight and demonstrates the critical need for light payloads to ensure maximum flight time. With time considerations for takeoff and landing, the Iris was capable of providing 4 min of on-site sampling flight time at a payload of 510 g. Although this initial sensor package was relatively light, future work will look to decrease the weight of the package in an attempt to increase total flight time and ensure a longer sampling duration per sample flight.

Future applications of UAS in atmospheric research will necessitate high vertical and horizontal flight precision for studies conducted within complex terrain, such as forest canopies or urban street canyons. During the vertical flight profiles, the altitude precision of the Iris drone relative to the programmed waypoint altitude was extremely high. The Iris drone was capable of holding within 0.35 m of the programmed altitude. Figure 3A demonstrates the vertical precision of the Iris drone for both replicate flights of Flight Plan A, with the drone flying as low as 5 m and as high as 100 m above sea level. The horizontal precision of the Iris drone was also high, with the Iris typically holding within 1 m of the pre-programmed location. The horizontal precision of the drone relative to the programmed waypoint position for all vertical profile flights is shown in Figure 3B. Overall, the drone demonstrated a high precision with regard to both vertical and horizontal position that showcases the potential utility of these sampling platforms for aerosol and trace-gas measurements in the boundary layer within various complex environments.

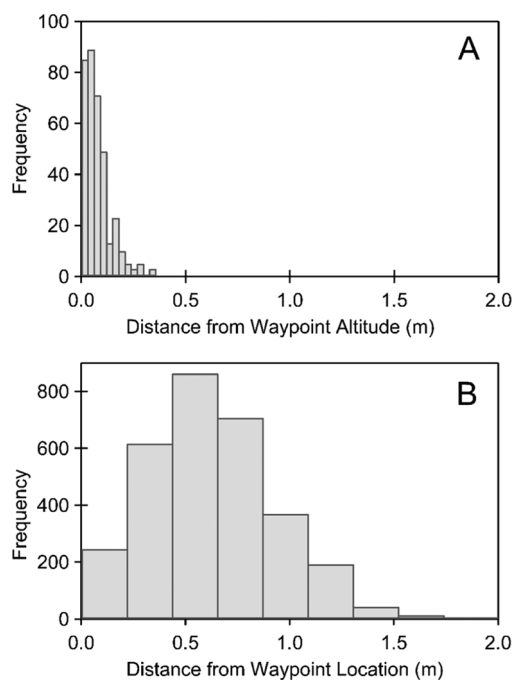


Figure 3. (A) Altitude precision of the Iris relative to the programmed waypoint altitude for both replicates of Flight Plan A. (B) Horizontal precision of the Iris relative to the programmed waypoint position for all vertical profile flights.

3.2. Surf-Zone Aerosol Production. Aerosol particle number concentrations were observed to be greater within and downwind of the surf-zone, consistent with previously reported observations of surf-zone enhancement.³¹ Production of sea-spray aerosol in the surf zone as compared to that in the near-open-ocean was observed in the horizontal profiles of aerosols measured along the Scripps Institution of Oceanography (SIO) pier on July 28th, 2015 (Figure 4) (additional information regarding the pier is provided in the Supporting Information). The horizontal profiles demonstrate that aerosol production in and downwind of the wave breaking region is significantly enhanced for both small and large particle channels in comparison to the aerosol concentrations over the open ocean, i.e., the end of the pier. In the large-particle-size channel, we observe enhancements by as much as a factor of 4.2 in the surf zone compared to results for the open ocean, and an enhancement factor of 2.3 in the small-particle concentration (Figure S3). The results agree with those presented by van Eijk et al.,³³ who reported a surf-zone enhancement factor of 3 to 5 for particles at smaller diameters ($0.5 \mu\text{m}$), increasing by a factor of 10 for larger particles ($10 \mu\text{m}$). The discrepancies between the magnitudes in the surf-zone enhancement between the studies is most likely due to differences in wind-wave energy dissipation in the surf zone, controlled by the bathymetry of the underlining surf zone and changes in the wave motion, the width of the breaker zone, and increased transport efficiency of the aerosol.^{32,36}

Furthermore, small and large particle measurements made along the pier on July 28th were highly correlated ($R^2 = 0.98$), with a slope of 5.29 ± 0.04 . Although the slope is higher than the ratio of small ($0.5 \mu\text{m} < d_p < 1 \mu\text{m}$) to large ($d_p > 1 \mu\text{m}$) particles measured for nascent sea spray (1.6) in an enclosed indoor wave channel,³⁷ it may be expected that the nascent sea-spray distribution would yield a shallower slope due to a longer lifetime of large particles in the wave-channel experiment

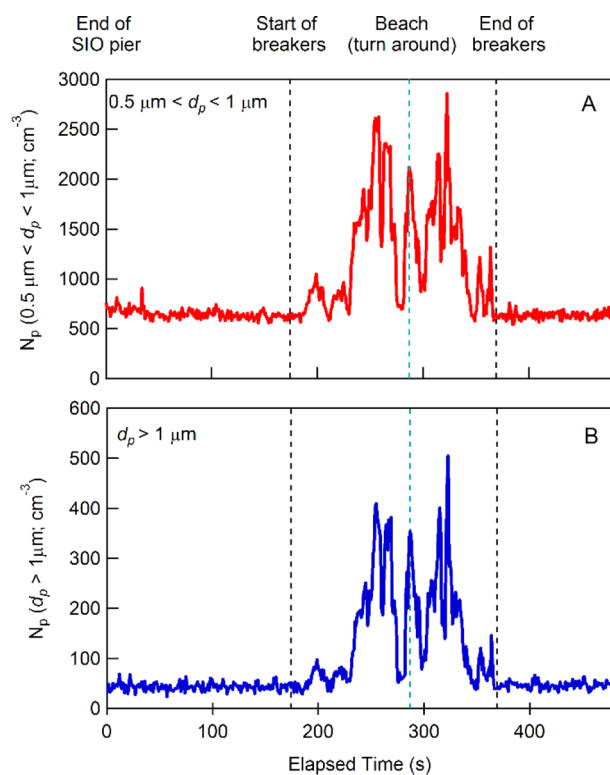


Figure 4. Time series of particle concentration measurements taken during mobile measurements that span the SIO pier on July 28, 2015.

relative to ambient conditions. Nonetheless, the surface observations provide confidence that the nascent sea spray aerosol production is clearly measurable with small-scale particle sensors.

3.3. Vertical and Horizontal Flight Profiles. A total of 13 separate vertical sampling flights were flown between July 29th and July 30th, 2015. The vertical sampling flights took place on the SIO beach and were flown according to the flight paths presented in Table 1 under the ambient conditions presented in Table 2. Multiple flight plans were flown to both assess the performance capabilities of the Iris as a sampling platform, discussed previously in section 3.1, as well as to effectively constrain the aerosol concentration measurements within the

first 100 m of the boundary layer. Figure 5 shows the mean particle concentrations ($\pm 1\sigma$) and CO₂ mixing ratios ($\pm 1\sigma$) for all 13 of the vertical flights sampled during this study. A maximum plume height of 30–35 m was observed and is in relatively good agreement with previously calculated surf-zone plume heights of 20–25 m presented by de Leeuw et al.³¹ and Hooper and Martin.³⁴ The CO₂ mixing ratio is consistent throughout the vertical column, within the precision of the K-30 CO₂ sensor (± 20 ppm), demonstrating a surf-zone aerosol source that is not directly influenced by isolated anthropogenic factors.

The vertical profile also demonstrates a turnover in the 0.5–1 μm particle concentrations at an altitude of 70 m. It is possible that the observed increase in small particle concentration may reflect the transition from the constant-flux surface layer to the mixed layer of the boundary layer. The surface layer typically accounts for the lowest 10% of the boundary layer and because a boundary layer height of 700 m is highly probable, an impact on aerosol concentration profiles at that transitional point would not be unexpected.³⁸ Although a more quantitative assessment of this turnover in the small particle concentration is outside of this work, it does provide an interesting science question that future flights and studies may be capable of addressing.

In addition to the vertical flights, horizontal flight profiles were also flown from the beach, over the surf zone. The horizontal flight paths were flown at 5, 10, 15, and 25 m to provide both horizontal and vertical measurements of the aerosol plume for comparison with measurements made along the SIO pier (Figure S7).

3.4. Surf-Zone Particle Emission Rate. Vertical profiles of the average small and large particle channels ($\pm 1\sigma$) located before and after the breaking waves were constructed from aerosol concentration data collected during the vertical and horizontal flights (Figure 6). Utilizing the vertical profiles in particle concentrations for both the open ocean and surf zone, we can calculate the SSA emission rate at the Scripps Pier using a column model. The mass balance equation for the time rate of change in particle number concentration (N_p) is defined as

$$\frac{d[N_p]}{dt} = \frac{E}{h} + P - L - D \quad (1)$$

Table 2. Average Meteorological and Swell Conditions for Each Individual Flight

flight	orientation	wind speed $\pm 1\sigma$ (m/s)	wind direction $\pm 1\sigma$ (deg)	air temperature $\pm 1\sigma$ (°C)	swell height $\pm 1\sigma$ (m)	swell period $\pm 1\sigma$ (s)
1	vertical	1.38 ± 0.02	265.03 ± 1.51	21.3 ± 0.02	0.63 ± 0.002	4.6 ± 0.005
2	vertical	1.57 ± 0.08	290.57 ± 0.20	22.1 ± 0.12	0.61 ± 0.002	4.5 ± 0.004
3	vertical	2.05 ± 0.04	282.46 ± 1.92	22.1 ± 0.08	0.63 ± 0.002	4.4 ± 0.004
4	vertical	2.59 ± 0.06	275.43 ± 1.75	21.6 ± 0.04	0.65 ± 0.002	4.4 ± 0.004
5	vertical	2.75 ± 0.02	270.06 ± 0.81	21.4 ± 0.08	0.67 ± 0.002	4.3 ± 0.004
6	vertical	2.81 ± 0.02	270.58 ± 0.42	21.3 ± 0.01	0.7 ± 0.00	5.0 ± 0.004
7	vertical	3.08 ± 0.09	272.74 ± 2.25	21.3 ± 0.01	0.7 ± 0.00	5.0 ± 0.003
8	vertical	3.20 ± 0.06	271.91 ± 0.63	21.3 ± 0.00	0.7 ± 0.00	4.9 ± 0.010
9	vertical	2.64 ± 0.05	259.72 ± 2.09	21.2 ± 0.01	0.7 ± 0.00	4.8 ± 0.010
10	vertical	2.69 ± 0.17	247.13 ± 0.75	21.3 ± 0.05	0.7 ± 0.00	4.7 ± 0.009
11	vertical	2.98 ± 0.07	266.69 ± 1.62	21.2 ± 0.01	0.7 ± 0.00	4.6 ± 0.009
12	vertical	2.11 ± 0.02	308.96 ± 1.51	22.6 ± 0.06	0.60 ± 0.001	4.5 ± 0.004
13	vertical	1.98 ± 0.07	296.54 ± 0.77	22.9 ± 0.05	0.58 ± 0.002	4.4 ± 0.006
14	horizontal	1.87 ± 0.06	305.78 ± 0.07	22.5 ± 0.01	0.50 ± 0.00	4.2 ± 7 × 10 ⁻⁴
15	horizontal	1.73 ± 0.02	305.65 ± 0.29	22.5 ± 0.00	0.50 ± 0.00	1.2 ± 9 × 10 ⁻⁴
16	horizontal	2.16 ± 0.03	309.87 ± 1.29	22.5 ± 0.00	0.50 ± 0.00	4.2 ± 9 × 10 ⁻⁴

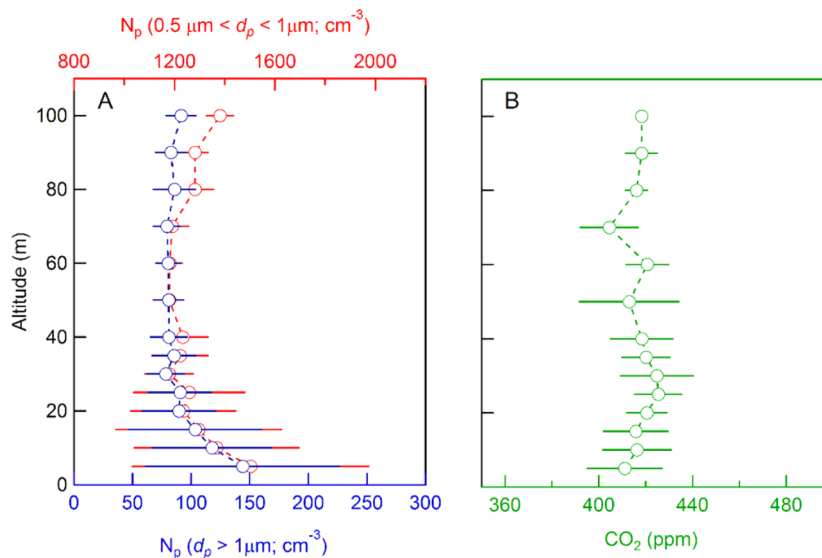


Figure 5. (A) Mean particle concentrations (and $\pm 1\sigma$) for the large (blue; $0.5 \mu\text{m} < d_p < 1 \mu\text{m}$) and small (red; $d_p > 1 \mu\text{m}$) size channels averaged for all 13 of the vertical flights sampled during this study. (B) Mean CO_2 mixing ratio (and $\pm 1\sigma$) for all 13 of the vertical flights sampled during this study.

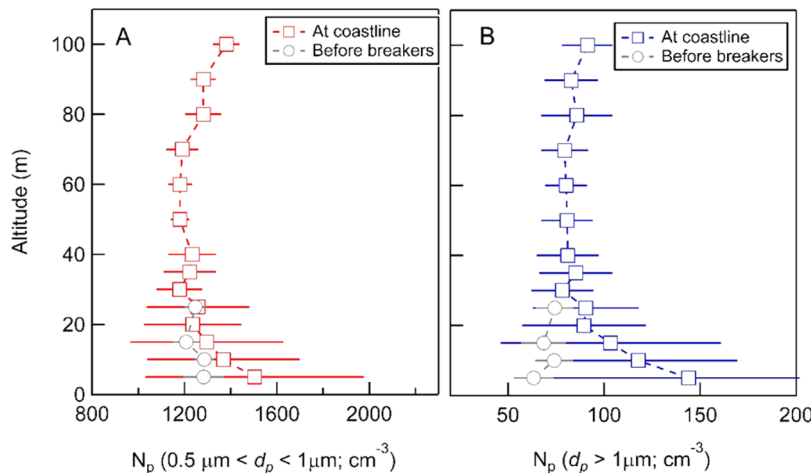


Figure 6. Vertical profiles of the average small (A) and large (B) particle channel counts $\pm 1\sigma$ located before (gray circles) and after (red or blue squares) the breaking waves.

where h is the mixing height of the column (27.5 m), P is the chemical production, L is the chemical loss, and D is deposition. Here we take P , L , and D to be zero and rearrange the equation using the chain rule to introduce U (mean wind speed; dx/dt).

$$\frac{d[N_p]}{dx} U = \frac{E}{h} \tag{2}$$

We can then solve for E with our measurement of $d[N_p]$, the change in the column averaged particle concentration, and dx , the length of the surf zone (here taken to be 30 m). We calculate aerosol particle emission rates for small and large particles in the surf zone to be 416 ± 729 and 187 ± 122 particles ($\text{cm}^{-2}\cdot\text{s}^{-1}$), respectively, at ambient humidity. We note that the large variability in the calculated emission rate, particularly for the small particles, is derived from the observed variance in particle number concentration (Figure 6). This variance reflects the strong temporal variability in the surf-zone emission source over the time period of sampling. Utilizing the

large channel particle flux and weighting mass calculations by a representative aerosol size distribution between 1 and $10 \mu\text{m}$ for a breaking wave,³⁷ we estimate an ambient humidity mass flux of 285 ± 61 ($\mu\text{g m}^{-2} \text{s}^{-1}$). This represents a conservative and potentially lower end estimation of mass flux, as influence of particles larger than $10 \mu\text{m}$ was not considered. The mass flux reported here is smaller than two previously reported literature values for the mass flux for Scripps Pier of 1500 ($\mu\text{g m}^{-2} \text{s}^{-1}$) [van Eijk et al.³³] and $562\text{--}1034$ ($\mu\text{g m}^{-2} \text{s}^{-1}$) [de Leeuw et al.³⁹]. In van Eijk et al.,³³ the mass flux is computed as a function of wave energy dissipation (WED), where the following relation between WED and the average wave height, H_{rms} was used:

$$\text{WED} = -3 + 35 \cdot H_{\text{rms}} \tag{3}$$

Using eq 3 we estimate that the WED during our study was approximately 20 Wm^{-2} , a factor of 1.6–2.6 smaller than the WED interval ($30\text{--}50 \text{ Wm}^{-2}$) for which van Eijk et al. presented their mass flux. Assuming the $3/4$ power dependence

between mass flux and WED, it is reasonable that we would observe a significant decrease in mass flux at our lower WED.

4. IMPLICATIONS FOR ATMOSPHERIC MEASUREMENTS

The primary objective of this work was the characterization of a quadrotor UAS as a sampling platform for near-surface (0–100 m) sampling of aerosol particle and trace gas distributions. The Iris demonstrated high precision in both vertical and horizontal positioning and showcased the future potential of these sampling platforms for measurements of aerosol and trace gas measurements within various complex environments in the boundary layer.

Utilizing the Iris sampling platform, vertical profile measurements of aerosol number were made between 5 and 100 m above the surf zone. The vertical profiles demonstrated a maximum aerosol plume height of 40 m above the surf zone. Based on the horizontal and vertical aerosol profiles measured in this work, ambient humidity emission rates for small and large particles in the surf zone were calculated to be 416 ± 729 and 187 ± 122 particles ($\text{cm}^{-2}\cdot\text{s}^{-1}$), respectively, with an estimated ambient humidity mass flux of 284 ± 61 ($\mu\text{g m}^{-2}\text{s}^{-1}$). The Iris UAS provided an efficient and precise sampling platform for measuring the vertical and horizontal profiles of sea spray aerosol generated within the boundary layer.

■ ASSOCIATED CONTENT

● Supporting Information

The Supporting Information is available free of charge on the ACS Publications website at DOI: [10.1021/acs.est.5b05320](https://doi.org/10.1021/acs.est.5b05320).

Further information regarding the sampling and surf zone aerosol production; Figure S1, representative vertical and horizontal flight plans; Figure S2, close-up and in-flight images of the Iris and sampling package; Figure S3, time series of particle concentrations measured at the SIO beach and terminal end of the SIO pier; Figure S4, frequency distributions of particle concentrations from continuous measurements at end of SIO pier and the beach at base of SIO pier; Figure S5, correlation of small and large particle measurements sampled during pier walk; Figure S6, research flight 1 particle concentration measurements; Figure S7, representative depiction of the horizontal flight profiles demonstrating particle channel counts. (PDF)

■ AUTHOR INFORMATION

Corresponding Author

*Phone: 608-890-3422; e-mail: timothy.bertram@wisc.edu.

Notes

The authors declare no competing financial interest.

■ ACKNOWLEDGMENTS

This publication was made possible by USEPA grant R835139. Its contents are solely the responsibility of the grantee and do not necessarily represent the official views of the USEPA. Furthermore, USEPA does not endorse the purchase of any commercial products or services mentioned in the publication.

■ REFERENCES

(1) IPCC Climate Change 2007: The physical science basis. *Contribution of Working Group I to the Fourth Assessment Report of*

the Intergovernmental Panel on Climate Change; Cambridge University Press: Cambridge, United Kingdom, 2007; p 996.

(2) Seinfeld, J. H.; Pandis, S. N. *Atmospheric Chemistry and Physics: From Air Pollution to Climate Change*. Wiley-Interscience: New York, NY, 1998.

(3) Pöschl, U. Atmospheric aerosols: composition, transformation, climate and health effects. *Angew. Chem., Int. Ed.* **2005**, *44* (46), 7520–40.

(4) Bernstein, J. A.; Alexis, N.; Barnes, C.; Bernstein, I. L.; Bernstein, J. A.; Nel, A.; Peden, D.; Diaz-Sanchez, D.; Tarlo, S. M.; Williams, P. B. Health effects of air pollution. *J. Allergy Clin. Immunol.* **2004**, *114* (5), 1116–23.

(5) Turóczy, B.; Hoffer, A.; Tóth, Á.; Kováts, N.; Ács, A.; Ferincz, Á.; Kovács, A.; Gelencsér, A. Comparative assessment of ecotoxicity of urban aerosol. *Atmos. Chem. Phys.* **2012**, *12* (16), 7365–7370.

(6) Lave, L. B.; Seskin, E. P. Analysis of association between United States mortality and air-pollution. *J. Am. Stat. Assoc.* **1973**, *68* (342), 284–290.

(7) Ma, X.; Yu, F. Seasonal variability of aerosol vertical profiles over east US and west Europe: GEOS-Chem/APM simulation and comparison with CALIPSO observations. *Atmos. Res.* **2014**, *140–141*, 28–37.

(8) Holton, J. R.; Hakim, G. J. *An Introduction to Dynamic Meteorology*. 5th ed.; Academic Press: Waltham, MA, 2013.

(9) O'Dowd, C. D.; Wagner, P. E. *Nucleation and Atmospheric Aerosols*: 17th International Conference, Galway, Ireland, 2007. 1st ed.; Springer: Netherlands, 2007.

(10) Sheridan, P. J.; Andrews, E.; Ogren, J. A.; Tackett, J. L.; Winker, D. M. Vertical profiles of aerosol optical properties over central Illinois and comparison with surface and satellite measurements. *Atmos. Chem. Phys.* **2012**, *12* (23), 11695–11721.

(11) Crawford, J. H.; Dickerson, R.; Hains, J., DISCOVER-AQ: Observations and early results. *Environ. Manag.*, Sep. **2014**, 8–15.

(12) Brown, S. S.; Thornton, J. A.; Keene, W. C.; Pszenny, A. A. P.; Sive, B. C.; Dubé, W. P.; Wagner, N. L.; Young, C. J.; Riedel, T. P.; Roberts, J. M.; VandenBoer, T. C.; Bahreini, R.; Öztürk, F.; Middlebrook, A. M.; Kim, S.; Hübler, G.; Wolfe, D. E. Nitrogen, Aerosol Composition, and Halogens on a Tall Tower (NACHTT): Overview of a wintertime air chemistry field study in the front range urban corridor of Colorado. *Journal of Geophysical Research: Atmospheres* **2013**, *118* (14), 8067–8085.

(13) Clarke, A. D.; Owens, S. R.; Zhou, J. An Ultrafine Sea-Salt Flux from Breaking Waves: Implications for Cloud Condensation Nuclei in the Remote Marine Atmosphere. *J. Geophys. Res.* **2006**, *111*, (D6).[10.1029/2005JD006565](https://doi.org/10.1029/2005JD006565)

(14) Petelski, T.; Piskozub, J. Vertical Coarse Aerosol Fluxes in the Atmospheric Surface Layer over the North Polar Waters of the Atlantic. *J. Geophys. Res.* **2006**, *111*, (C6).[10.1029/2005JC003295](https://doi.org/10.1029/2005JC003295)

(15) Petelski, T. Marine aerosol fluxes over open sea calculated from vertical concentration gradients. *J. Aerosol Sci.* **2003**, *34* (3), 359–371.

(16) Hara, K.; Osada, K.; Yamanouchi, T. Tethered balloon-borne aerosol measurements: seasonal and vertical variations of aerosol constituents over Syowa Station, Antarctica. *Atmos. Chem. Phys.* **2013**, *13* (17), 9119–9139.

(17) Holland, G. J.; Webster, P. J.; Curry, J. A.; Tyrell, G.; Gauntlett, D.; Brett, G.; Becker, J.; Hoag, R.; Vaglianti, W. The aerosonde robotic aircraft: A new paradigm for environmental observations. *Bull. Am. Meteorol. Soc.* **2001**, *82*, 889–901.

(18) Clarke, A. D.; Ahlquist, N. C.; Howell, S.; Moore, K. A miniature optical particle counter for in situ aircraft aerosol research. *Journal of Atmospheric and Oceanic Technology* **2002**, *19* (10), 1557–1566.

(19) Ramanathan, V.; Ramana, M. V.; Roberts, G.; Kim, D.; Corrigan, C.; Chung, C.; Winker, D. Warming trends in Asia amplified by brown cloud solar absorption. *Nature* **2007**, *448* (7153), 575–8.

(20) Bates, T. S.; Quinn, P. K.; Johnson, J. E.; Corless, A.; Brechtel, F. J.; Stalin, S. E.; Meinig, C.; Burkhardt, J. F. Measurements of atmospheric aerosol vertical distributions above Svalbard, Norway,

using unmanned aerial systems (UAS). *Atmos. Meas. Tech.* **2013**, *6* (8), 2115–2120.

(21) Buzorius, G.; Kalogiros, J.; Varutbangkul, V. Airborne aerosol flux measurements with eddy correlation above the ocean in a coastal environment. *J. Aerosol Sci.* **2006**, *37* (10), 1267–1286.

(22) Li, J.; Yin, Y.; Li, P.; Li, Z.; Li, R.; Cribb, M.; Dong, Z.; Zhang, F.; Li, J.; Ren, G.; Jin, L.; Li, Y. Aircraft measurements of the vertical distribution and activation property of aerosol particles over the Loess Plateau in China. *Atmos. Res.* **2015**, *155*, 73–86.

(23) Hara, K.; Iwasaka, Y.; Wada, M.; Ihara, T.; Shiba, H.; Osada, K.; Yamanouchi, T. Aerosol Constituents and Their Spatial Distribution in the Free Troposphere of Coastal Antarctic Regions. *J. Geophys. Res.* **2006**, *111*, (D15).[10.1029/2005JD006591](https://doi.org/10.1029/2005JD006591)

(24) Li, X.; Rohrer, F.; Hofzumahaus, A.; Brauers, T.; Haseler, R.; Bohn, B.; Broch, S.; Fuchs, H.; Gomm, S.; Holland, F.; Jäger, J.; Kaiser, J.; Keutsch, F. N.; Lohse, I.; Lu, K.; Tillmann, R.; Wegener, R.; Wolfe, G. M.; Mentel, T. F.; Kiendler-Scharr, A.; Wahner, A. Missing gas-phase source of HONO inferred from Zeppelin measurements in the troposphere. *Science* **2014**, *344* (6181), 292–296.

(25) Stokes, M. D.; Deane, G. B.; Prather, K.; Bertram, T. H.; Ruppel, M. J.; Ryder, O. S.; Brady, J. M.; Zhao, D. A Marine Aerosol Reference Tank system as a breaking wave analogue. *Atmospheric Measurement Techniques Discussions* **2012**, *5* (6), 8701–8728.

(26) Cipriano, R. J.; Monahan, E. C.; Bowyer, P. A.; Woolf, D. K. Marine condensation nucleus generation inferred from whitecap simulation tank results. *J. Geophys. Res.* **1987**, *92* (C6), 6569.

(27) Blanchard, D. C. The production, distribution and bacterial enrichment of the sea-salt aerosol. In *Air-Sea Exchange of Gases and Particles*; Liss, P. S.; Slinn, W. G. N., Eds. D. Reidel: Norwell, Mass., 1983; pp 407–454.

(28) Blanchard, D. C. Positive Space Charge from the Sea. *J. Atmos. Sci.* **1966**, *23* (5), 507–515.

(29) Quinn, P. K.; Collins, D. B.; Grassian, V. H.; Prather, K. A.; Bates, T. S. Chemistry and related properties of freshly emitted sea spray aerosol. *Chem. Rev.* **2015**, *115* (10), 4383–99.

(30) Monahan, E. C. *Coastal Aerosol Workshop Proceedings*; Monterey, CA, 1995.

(31) de Leeuw, G.; Neele, F. P.; van Eijk, A. M. J.; Vignati, E.; Hill, M.; Smith, M. H. Aerosol production in the surf zone and effects on IR extinction. *Proc. SPIE* **1997**, *3125*, 14.

(32) Chomka, M.; Petelski, T. Modelling the sea aerosol emission in the coastal zone. *Oceanologia* **1997**, *39* (3), 211–225.

(33) van Eijk, A. M. J.; Kusmierczyk-Michulec, J. T.; Francius, M. J.; Tedeschi, G.; Piazzola, J.; Merritt, D. L.; Fontana, J. D. Sea-spray aerosol particles generated in the surf zone. *J. Geophys. Res.* **2011**, *116*, (D19).[10.1029/2011JD015602](https://doi.org/10.1029/2011JD015602)

(34) Hooper, W. P.; Martin, L. U. Scanning lidar measurements of surf-zone aerosol generation. *Opt. Eng.* **1999**, *38* (2), 250–255.

(35) Mission Planner. <http://planner.ardupilot.com> (accessed Sep 1, 2015).

(36) Neele, F. P.; de Leeuw, G.; Jansen, M.; Stive, M. Quantitative assessment of surf-produced sea spray aerosol. *Proc. SPIE* **1998**, *3433*, 53–62.

(37) Prather, K. A.; Bertram, T. H.; Grassian, V. H.; Deane, G. B.; Stokes, M. D.; Demott, P. J.; Aluwihare, L. I.; Palenik, B. P.; Azam, F.; Seinfeld, J. H.; Moffet, R. C.; Molina, M. J.; Cappa, C. D.; Geiger, F. M.; Roberts, G. C.; Russell, L. M.; Ault, A. P.; Baltrusaitis, J.; Collins, D. B.; Corrigan, C. E.; Cuadra-Rodriguez, L. A.; Ebben, C. J.; Forestieri, S. D.; Guasco, T. L.; Hersey, S. P.; Kim, M. J.; Lambert, W. F.; Modini, R. L.; Mui, W.; Pedler, B. E.; Ruppel, M. J.; Ryder, O. S.; Schoepp, N. G.; Sullivan, R. C.; Zhao, D. Bringing the ocean into the laboratory to probe the chemical complexity of sea spray aerosol. *Proc. Natl. Acad. Sci. U. S. A.* **2013**, *110* (19), 7550–5.

(38) Stull, R. B. *An Introduction to Boundary Layer Meteorology*, Reprint ed.; Springer: Dordrecht, 2009; p 670 pages.

(39) de Leeuw, G.; Neele, F. P.; Hill, M.; Smith, M. H.; Vignati, E. Production of sea spray aerosol in the surf zone. *J. Geophys. Res.* **2000**, *105* (D24), 29397.